Available online at www.sciencedirect.com
SCIENCE DIRECT®
Journal of Nuclear Materials 324 (2004) 6–22
journal of nuclear materials
www.elsevier.com/locate/jnucmat

Structure of zirconium alloy oxides formed in pure water studied with synchrotron radiation and optical microscopy: relation to corrosion rate

Aylin Yilmazbayhan [a], Arthur T. Motta [a,*], Robert J. Comstock [b], George P. Sabol [c], Barry Lai [d], Zhonghou Cai [d]

[a] *Department of Mechanical and Nuclear Engineering, The Pennsylvania State University, University Park, PA 16802, USA*
[b] *Science and Technology Department, Westinghouse Electric Co., 1340 Beulah Rd, Pittsburgh, PA, USA*
[c] *Consultant to Westinghouse Electric Co., 1340 Beulah Rd, Pittsburgh, PA, USA*
[d] *Advanced Photon Source, XFD 401 B3194, Argonne National Laboratory, 9700 South Cass Ave., Argonne, IL 60439, USA*

Received 4 April 2003; accepted 22 August 2003

Abstract

A detailed study was undertaken of oxides formed in 360 °C water on four Zr-based alloys (Zircaloy-4, ZIRLO™, [1] Zr–2.5%Nb and Zr–2.5%Nb–0.5%Cu) in an effort to relate oxide structure to corrosion performance. Micro-beam X-ray diffraction was used along with transmitted light optical microscopy to obtain information about the structure of these oxides as a function of distance from the oxide–metal interface. Optical microscopy revealed a layered oxide structure in which the average layer thickness was inversely proportional to the post-transition corrosion rate. The detailed diffraction studies showed an oxide that contained both tetragonal and monoclinic ZrO_2, with a higher fraction of tetragonal oxide near the oxide–metal interface, in a region roughly corresponding to one oxide layer. Evidence was seen also of a cyclic variation of the tetragonal and monoclinic oxide across the oxide thickness with a period of the layer thickness. The results also indicate that the final grain size of the tetragonal phase is smaller than that of the monoclinic phase and the monoclinic grain size is smaller in Zircaloy-4 and ZIRLO than in the other two alloys. These results are discussed in terms of a model of oxide growth based on the periodic breakdown and reconstitution of a protective layer.

1. Introduction

For the last decade, the corrosion behavior of Zr-based alloys has been at the forefront of LWR fuel technology. The corrosion resistance of fuel cladding and structural components often limits economic improvements in fuel utilization, such as those associated with higher heat fluxes, fluid temperatures and core residence times. This challenge to fuel performance has been addressed in the past through optimization of the chemistry and microstructure of the existing commercial alloys, Zircaloy-2 and -4 and the Zr–1.0% and –2.5%Nb alloys, and introduction of alloys containing both Sn and Nb [1,2]. This empirical development has resulted in the correlation of alloy microstructure with corrosion behavior and in practical thermo-mechanical processing schemes for achieving optimum corrosion response. It is now well established that corrosion resistance of Zircaloy-4 in pressurized water reactors (PWR) is improved when the size of the second-phase particles (SPPs) is greater than about one-tenth micron [3] and the tin content is in the low range of the specification [4,5]. In

---

[*] Corresponding author. Tel.: +1-814 865 0036; fax: +1-814 865 8499.

E-mail address: atm2@psu.edu (A.T. Motta).

[1] ZIRLO is a trademark of Westinghouse Electric Co.

0022-3115/$ - see front matter © 2003 Elsevier B.V. All rights reserved.
doi:10.1016/j.jnucmat.2003.08.038

contrast, small SPP size (less than one-tenth micron) is needed for maximum corrosion resistance of the 1.0% and 2.5%Nb alloys [6,7] and also for ZIRLO [1]. Small SPP size is also needed in the Zircaloys for resistance to nodular corrosion in boiling water reactors (BWRs). The mechanisms for such corrosion improvements are not well understood.

As a result of the already extensive optimization of the existing alloys, it is believed that further significant improvement in corrosion resistance requires a more mechanistic understanding of the corrosion process to allow selective emphasis on those characteristics favorable to superior corrosion behavior. Therefore, a fundamental understanding of the structural development and properties of the oxide layer is needed. Efforts to provide such fundamental data have been ongoing for some time [8–10]. Unfortunately, many of the studies focus on a limited set of oxide features, or are limited by alloy availability. In addition, the resolution limits of the experimental techniques are often insufficient for detection of significant effects.

The commonly accepted macroscopic description of the corrosion kinetics of zirconium-based alloys in aqueous media divides the total process into two regimes [11–13]. An initial pre-transition region that is approximately parabolic with respect to time is followed by a post-transition region of more accelerated kinetics with an approximately linear dependence on time. The onset of the accelerated corrosion regime is called the 'oxide transition' and is characterized by either the exposure time or by the oxide thickness at which the change in kinetics occurs. However, in reviewing the corrosion data with more scrutiny, it is observed that this simple description of the kinetics is only an approximation. The kinetics in pre-transition are not parabolic, but display a cubic dependence on time [14,15]. More importantly, the post-transition regime is composed of several periods of corrosion that mimic pre-transition kinetics in a cyclical sequence. On individual samples, the cyclic nature of the kinetics can be easily distinguished through several repetitions. The cyclic nature of post-transition corrosion has been observed and noted for some time [16,17] and observations [8,9,18,19] of stratification in the oxide films have been correlated with the cyclic kinetics.

Acknowledging that oxide growth results from oxygen migration through the oxide, the rate of oxidation may be controlled by either the ionic or electronic conductivity of the oxide layer. For pure zirconium, evidence [13,20] indicates that electronic conductivity is rate controlling at PWR fuel cladding temperatures, 290–400 °C. For the oxide formed on Zircaloy-2, on the other hand, electric potential measurements across the oxide indicate corrosion rate control by ionic transport processes. For the Zr–2.5%Nb alloy the relative importance of ionic and electronic processes depends upon the metallurgical structure of the alloy. For material with a fine distribution of β-Nb precipitates (quenched and aged) for which the corrosion resistance is very good, ionic transport is rate controlling at the temperatures of interest. It has also been suggested [20,21] that relative changes in the ionic and electronic conductivity caused by irradiation, such as fast neutron damage of the oxide and radiolysis of the coolant, may be responsible for in-reactor accelerated corrosion. Regardless of the role of electronic conduction in the corrosion kinetics, the extent of corrosion results from the mass transfer of oxygen through the oxide layer and subsequent conversion to more oxide at the metal/oxide interface. Furthermore, for out-reactor post-transition corrosion of alloys of commercial significance, it is generally believed that ionic transport of oxygen through the oxide layer controls corrosion kinetics.

From studies of the nature of the oxide films, a significant number of oxide features have been identified. The oxides are a mixture of the stable monoclinic ZrO_2 phase and a tetragonal ZrO_2 phase, the latter stabilized by local conditions in the oxide, such as stresses, small grain size and dissolved alloying elements [22]. The grain morphology consists of a mixture of equiaxed and columnar grains [23–26] and it has been proposed that the columnar grains are protective [27,28]. These oxides are known to develop cracking and porosity during their growth, which various researchers have linked to the transition in kinetics [9,18,29]. The SPPs present in the base metallic alloy are incorporated unoxidized into the oxide layer and only undergo oxidation after some residence time in the oxide [30,31], which some researchers have associated with the onset of oxide transition [26]. There is a clear degradation of corrosion behavior when the oxides are formed in lithiated water. It has been proposed [27] that the effect of Li is to destroy the inner barrier layer by preventing development of the columnar structure. Instead, equiaxed grains are formed that are less protective.

Thus, there is considerable data on oxide observations. However, conflicting data prevent further extrapolation of the observations into a mechanistic model for corrosion. For example, oxides formed on Zr–Sn–Fe–Cr alloys with high tin content have been reported as having both lower [23] and higher [32] tetragonal phase content compared with similar alloys with lower tin. Columnar grains have been normally associated with the monoclinic phase [33] but other researchers have shown that columnar tetragonal grains also form [25], as well as monoclinic equiaxed grains [34]. Thus, as mentioned in recent comprehensive reviews [33,35,36] of the subject, there currently is no unified model or overall mechanistic understanding of the oxide growth in Zr-based alloys.

The purpose of this investigation is to provide additional insight into the relationship between the structure of the oxide layers formed on Zr-based alloys and the resulting corrosion behavior. Four alloys, Zircaloy-4, ZIRLO, Zr–2.5%Nb and Zr–2.5%Nb–0.5% Cu, are selected for study based upon the large variation in their post-transition corrosion rates in 360 °C pure water. The high brilliance of the X-ray beam from the synchrotron source allow data acquisition with a lateral resolution heretofore unobtainable. The oxide structures are characterized by microbeam X-ray diffraction that permits the study of oxide structure as a function of distance from the oxide–metal interface. These new methods, in combination with more classical techniques of materials characterization, are used to differentiate microstructural features of the oxides on the four alloys. A comparison is made of the oxide features with the corrosion kinetics of the alloys and with other data in the literature.

2. Experimental methods

2.1. Alloy materials

Tubing was fabricated from sponge-based ingots of four zirconium alloys: Zircaloy-4, ZIRLO, Zr–2.5%Nb and Zr–2.5%Nb–0.5%Cu. The chemical analysis of the ingots is shown in Table 1. All tubing was in the cold-worked and stress–relief annealed condition.

2.2. Corrosion tests

Long-term corrosion testing of tubing specimens approximately 20 mm long from the four Zr-based alloys was performed in 360 °C water at saturation pressure. The testing was performed in a manner consistent with ASTM G2-88 [Standard Test Method for Corrosion Testing of Products of Zirconium, Hafnium and Their Alloys in Water at 680 °F (360 °C) or in Steam at 750 °F (400 °C)]. Multiple specimens from each alloy were corrosion tested simultaneously in a single autoclave with the test being periodically interrupted to measure specimen weight gain as a function of exposure time. The maximum exposure for the alloys was 784 days.

2.3. Optical microscopy

Samples for optical light microscopy were small transverse cross-sections of tubing that were prepared according to the following procedure. Axial segments of about 1.5 mm width were cut from the tubular corrosion samples and then ground to a thickness of about 0.35 mm from the inner diameter surface to facilitate subsequent insertion into a 3 mm diameter brass tube. Care was taken to provide backing to the outer diameter oxide for subsequent grinding and polishing. This was accomplished in one of two ways. The outer diameter oxide was placed next to either a silicon wafer or to the outer diameter oxide from a second axial slice. The silicon wafer composite samples were then inserted directly into a brass tube and bonded in place using Gatan G1 epoxy. The samples without the silicon wafer were glued together, inserted into a slit in a brass rod which was then inserted into a brass tube and bonded with epoxy. Slices about 0.5 mm thick were then cut from the brass tube to provide 3 mm diameter disks with the oxide cross-section located near the center of the disk.

The disk samples were ground on 600 grit silicon carbide paper on both sides until the thickness was approximately 100 μm. These disks were then dimpled by use of a Gatan Model 656 Dimple Grinder with the dimple centered near the oxide–silicon or oxide–oxide interface. The dimple was made by using progressively finer diamond abrasives followed by a final polish using 0.05 μm alumina. Dimples were made on both sides of the disk with the final thickness of the disk at the bottom of the dimple in the range of 5–8 μm. At this range of thickness, light was transmitted through the oxide and the layered structure was apparent. Throughout sample preparation and polishing, care was constantly exercised to avoid sample deformation and to remove the damaged oxide from the cutting operation because of the sensitivity of the oxide to develop lateral cracks during preparation [19,29]. In most of the alloys, the layered structure was not visible, or just vaguely visible when viewed in reflected light. Further characterization of these bands was performed in the scanning electron microscope (SEM).

Table 1
Chemical composition of zirconium alloy ingots (wt ppm)

Element	Zircaloy-4 (nominal)	ZIRLO	Zr–2.5%Nb	Zr–2.5%Nb–0.5%Cu
Sn	15 000	9600	10	<10
Nb	–	9900	25 500	24 300
Fe	2100	1000	504	385
Cr	1000	<50	51	<50
O	1300	1430	1330	1365
Cu	–	<25	<25	4700

2.4. Synchrotron radiation experiments

Experiments were performed at the 2ID-D beamline of the Advanced Photon Source (APS) at Argonne National Laboratory. Using zone plate diffraction gratings, the X-ray microprobe in the experimental station produces an monochromatic X-ray beam of size 0.2 μm × 0.3 μm with a photon flux of 5×10^9 photons/sec with an X-ray energy band width (dE/E) of 0.01% [37]. The focal spot size was measured from the X-ray fluorescence profile obtained from a Cr knife edge while it was scanned across the X-ray beam. The focal plane of the zone plate optics was adjusted so that the minimum spot size was obtained and the focal spot was at the surface of the specimen. For the present experiments, an asymmetric focusing configuration was adopted, in which the beam was focused down to 0.25 μm in the vertical direction corresponding to the direction normal to the oxide–metal interface and to about 2 μm in the horizontal direction (parallel to the oxide–metal interface) in order to sample a larger volume of the specimen. Fig. 1 shows the scattering and data acquisition geometry for the synchrotron radiation experiments: the microbeam is incident on the region of interest of the specimen and the scattering intensity in a section of reciprocal space is captured by a flat, two-dimensional detector (CCD camera). Samples for the synchrotron radiation experiments were prepared in a similar manner as those used for optical microscopy (0.5 mm thick slices of the brass tubes). The side of the disk that was examined received a final mechanical polish to 0.3 μm diamond followed by 0.05 μm alumina. The beam energy was 9.5 keV, corresponding to a wavelength of 0.1305 nm.

The position of the oxide–metal and oxide–water interfaces was found by monitoring Zr fluorescence counts as the sample was translated across the beam, as shown in Fig. 2. The distance between the oxide–metal interface and the oxide–water interface measured by this method was in good agreement with optical determination of the oxide thickness, to within 0.5 μm.

2.5. Processing and integration of synchrotron results

Because the CCD camera was not perpendicular to the incident beam direction, the intersections of the diffraction cones with the plane of the CCD were sections of ellipses, not circles. The digital data were integrated over the elliptical sections for a fixed angle ‘pie slice’ or constant azimuthal angular range to provide intensity versus two-theta data. Lorentz and polarization factors were then applied to these integrated data. The Lorentz correction factor includes three different terms [38], one of which was applied during the integration. Because the synchrotron beam is 99% polarized in the direction perpendicular to the oxide–metal interface, the polarization factor is $0.01 + 1.99\cos^2 2\theta$. As a result, the intensity correction from the combined Lorentz–Polarization (LP) factor is given by:

$$I^{\text{corr}} = \frac{I^{\text{int}}}{(\text{LP})}; \quad \text{where LP} = \frac{(0.01 + 1.99\cos^2 2\theta)}{\sin\theta}. \tag{1}$$

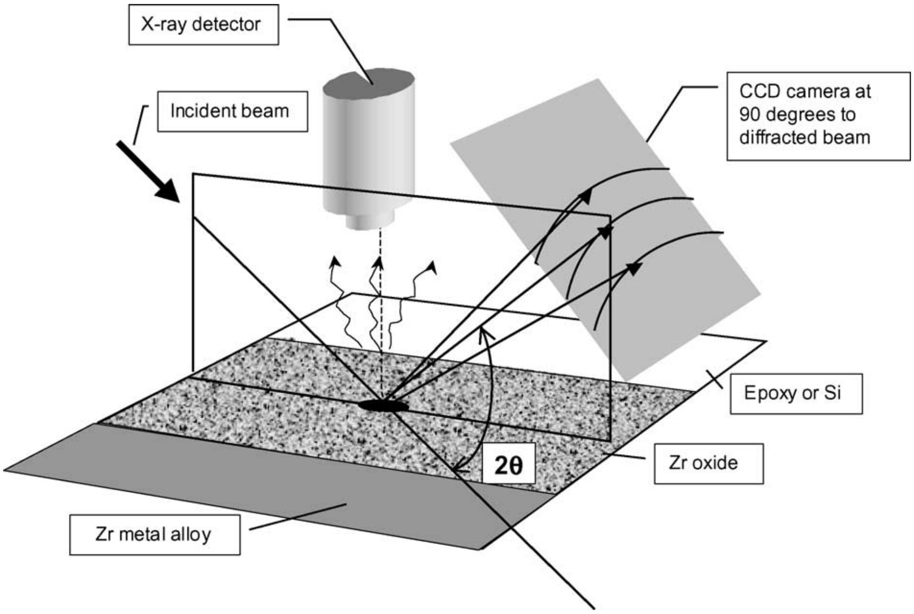

Fig. 1. Schematic drawing showing the geometry of data acquisition at the synchrotron beamline.

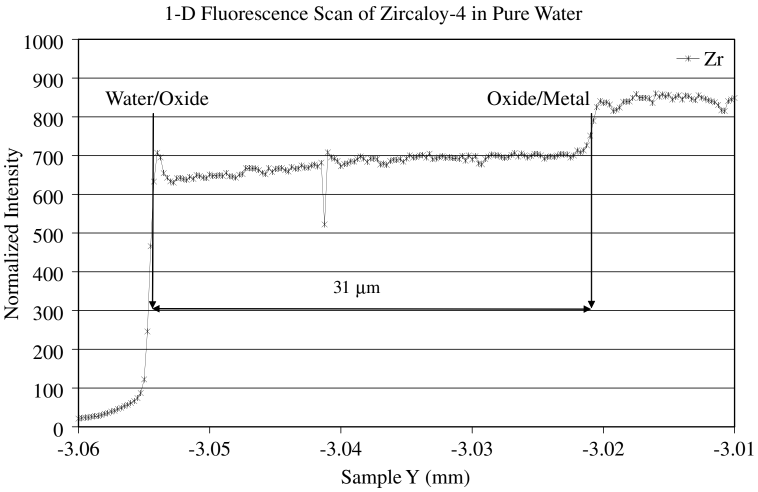

Fig. 2. Fluorescence scan of Zr showing oxide location in a Zircaloy-4 corrosion sample, exposed to 360 °C water for 784 days.

Following the integration and above corrections, a plot of diffracted intensity versus two-theta angle was obtained at each location analyzed.

3. Results

3.1. Corrosion data

Fig. 3(a) shows the weight gain versus exposure time in 360 °C pure water for the four alloys studied in this work. The oxidation curves initially follow either parabolic or cubic kinetics with the first cycle of oxidation ending with the occurrence of the oxide transition normally associated with the loss of protectiveness of the oxide. Oxidation then continues with additional cycles of parabolic or cubic weight gain kinetics. This initial transition in kinetics is readily identified in Fig. 3(b) (enlarged view of Fig. 3(a)). At later times, this cyclic pattern of parabolic or cubic kinetics, although still visible, becomes less pronounced. While the cause of this transition has not yet been determined, it is thought to be related to the accumulation of stress in the oxide and subsequent development of large-scale cracking or porosity [8,19,22,39] although other views exist [29]. It is also clear from Fig. 3(b) that, prior to the first transition, the corrosion kinetics of the four alloys are similar.

It is clear from the figure that the alloys differ in their post-transition corrosion rates, with Zircaloy-4 having the highest corrosion rate, followed by ZIRLO, Zr–2.5%Nb and Zr–2.5%Nb–0.5%Cu. These rates are tabulated in Table 2 along with the total oxide thickness following 784 days of testing. The exposure times and oxide thicknesses at the first oxide transition, as determined from the weight gain curves, are also shown in Table 2. These times and thicknesses at transition should be considered estimates since data were obtained only at

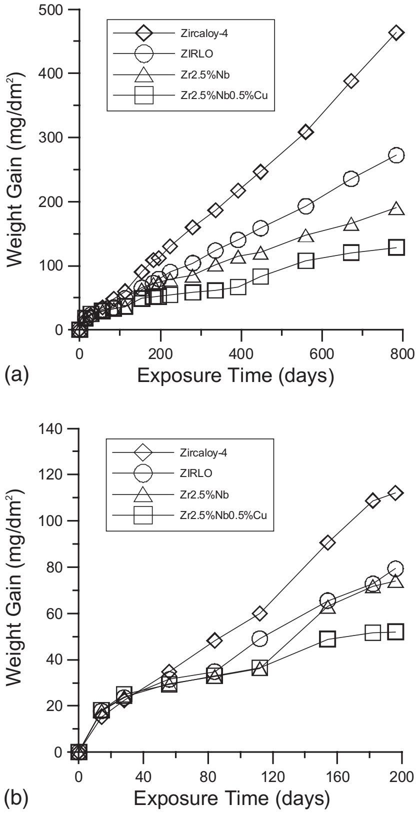

Fig. 3. Weight gain in mg/dm^2 versus exposure time for the corrosion of Zircaloy-4, ZIRLO, Zr–2.5%Nb and Zr–2.5%Nb–0.5%Cu in pure water at 360 °C (a) showing 784 days and (b) showing initial 200 days.

Table 2
Corrosion results following 784 days in 360 °C pure water

Alloy	First Transition		Total oxide[a] (µm)	Post transition corrosion rate (mg/dm^2/d)	Average layer thickness (µm)
	Time (days)	Oxide (µm)[a]			
Zircaloy-4	28	1.50	30.9	0.58	1.82
ZIRLO	84	2.32	18.1	0.33	2.01
Zr–2.5%Nb	112	2.41	12.7	0.21	2.54
Zr–2.5%Nb-0.5%Cu	112	2.43	8.6	0.14	2.87

[a] Thickness estimated from weight gain using relationship of 1 µm = 15 mg/dm^2.

discrete times. However, it is clear that the post-transition corrosion rates tend to decrease as the time to transition (or oxide layer thickness at transition) increases. This will be discussed in more detail below.

3.2. Optical and scanning electron microscopy

Fig. 4 shows optical micrographs of the transverse cross-sections of the corrosion oxide films on the four alloys after 784 days of exposure in 360 °C water. The final surface preparation is as-polished with 0.05 µm alumina on both sides of the sample. The oxide on Zircaloy-4 is 31 µm thick. The stratification of the oxide can be seen in the transmitted light micrograph, Fig. 4(b), but is not visible in the reflected light micrograph, Fig. 4(a). The continuity of the individual strata can be clearly followed. It is also observed that the thickness of each layer in the oxide is approximately the same. For this sample, seventeen layers were counted, indicating an average layer thickness of 1.82 µm.

The well-defined stratification was seen in all of the oxides formed during exposure in 360 °C water. Micrographs of the oxides on ZIRLO, Zr–2.5%Nb and the Zr–2.5%Nb–0.5%Cu alloy are shown in Fig. 4(c)–(h), respectively. For the 784-day exposure, the number of layers decreased and the thickness of the layers increased with a decrease in total oxide thickness. The average layer thickness was calculated by dividing the total oxide thickness (as determined from the weight gain data) by the number of layers. This latter value was taken as the number of bright lines in the transmitted light micrographs plus one, because it appeared that the actively growing interface was a dark and not a bright, optically active zone in the micrographs. That is, the more optically transparent bright lines separated the thicker more optically opaque layers in the oxide. The average thickness of the oxide layers in the four alloys is given in Table 2. The layers observed in transmitted light were also observed in polarized light, albeit less clearly. Nevertheless, it was possible to establish a 1:1 correlation in the stratification of the oxides by use of both methods of optical illumination. Stratification of oxide corrosion films as observed in polarized light has been reported previously [9,10,19,29]. Possible reasons for this optical contrast are discussed in Section 4.

Additional characterization of the oxide samples was performed by use of scanning electron microscopy. Both the secondary and backscattered electron modes of imaging are shown for the Zr–2.5%Nb sample and clear indications of the layered oxide structure could be observed (Fig. 5). The layers could be resolved in both SEM modes but the contrast was enhanced in the backscattered electron mode, consistent with the use of this mode to delineate cracks in oxide cross sections formed on Zircaloy-4 [40]. As with transmitted light and polarized reflected light micrographs of this sample, five discrete layers are seen in the oxide. The four boundaries giving the dark contrast in the SEM correspond to the bright boundaries (high light transmission) in the transmitted light micrographs. The SEM micrographs, however, indicate that these boundaries are not continuous, but rather consist of numerous individual sites of different contrast forming bands that are aligned parallel to the metal/oxide interface. With this morphology, it is clear that these microstructural features are not cracks as observed and described in numerous publications, for example, Bossis et al., [40] but represent some other microstructural feature as previously suggested [19,29].

3.3. Microdiffraction studies of oxides

Using the X-ray microbeam at APS, systematic scans, from the oxide–metal to the oxide–water interface were performed to study the variations in oxide crystal structure and composition as a function of position in the oxide. Fluorescence and diffraction data were simultaneously acquired using the setup schematically shown in Fig. 1. Fig. 6 shows a fully indexed diffraction pattern (intensity versus two-theta angle) taken from an oxide formed in a ZIRLO sample at a location approximately 1.25 µm from the oxide–metal interface and integrated according to the procedure described in Section 2. The diffraction peaks are identified in Table 3.

The identified phases were hcp–Zr, monoclinic ZrO_2 and tetragonal ZrO_2. Occasionally near the oxide–metal

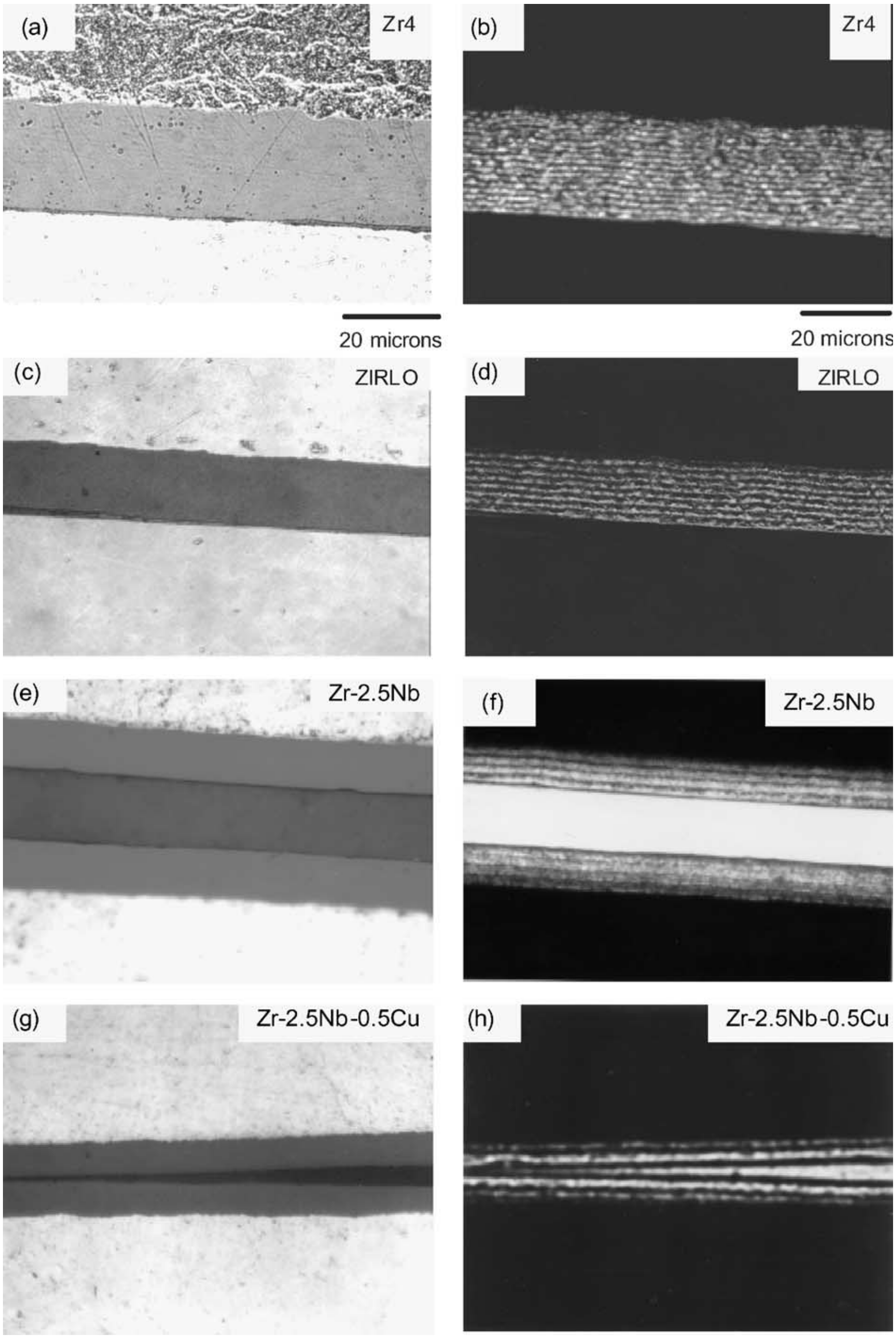

Fig. 4. Optical micrographs, in reflected and transmitted light for oxides formed in 360 °C water for 784 days (a,b) Zircaloy-4, (c,d) ZIRLO, (e,f) Zr–2.5%Nb, (g,h) Zr–2.5%Nb–0.5%Cu.

interface, diffraction peaks were observed that could be indexed as zirconium hydride. The agreement between the literature values and the indexed peaks is excellent, allowing for positive identification of the phases. The only exception was the tetragonal oxide peak, which was located in a two-theta position that corresponded neither to the (1 0 1) tetragonal peak nor to the (1 1 1) cubic peak. This is consistent with the results of Petigny et al. [41] who also observed a peak in the same location and which they identified as tetragonal. Other researchers

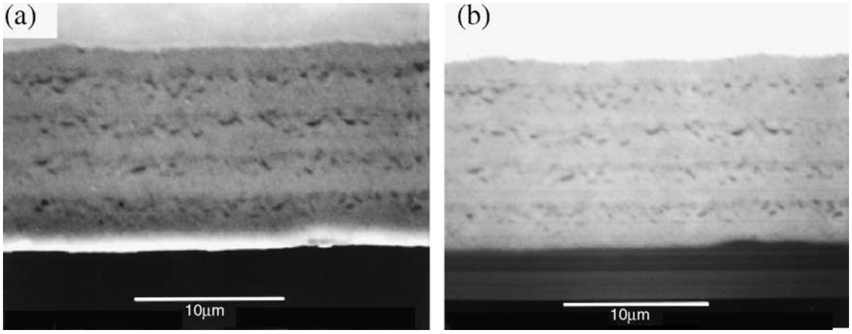

Fig. 5. (a) Secondary and (b) backscattered scanning electron images of oxide formed on Zr–2.5%Nb alloy exposed to 360 °C water for 784 days.

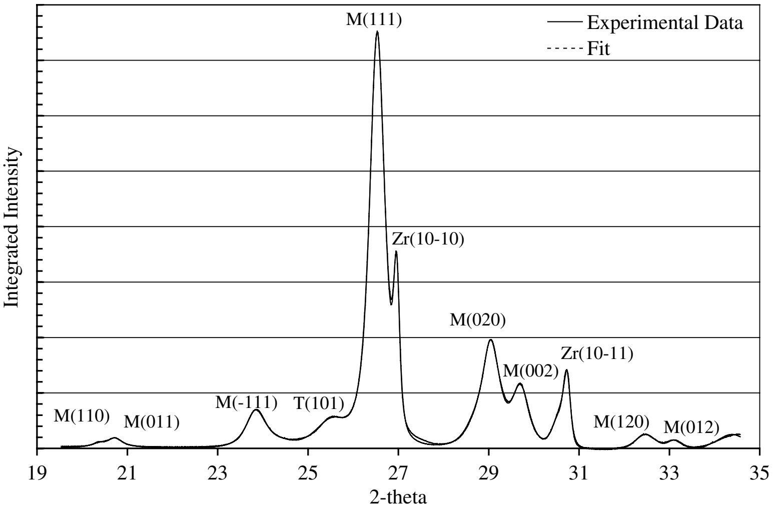

Fig. 6. Indexed diffracted pattern from oxide at 1.25 μm from the oxide–metal interface of a ZIRLO sample exposed to 360 °C water for 784 days.

Table 3
Comparison of measured peak locations to literature values

Peak indexing	Observed 2θ	JCPDF 2θ
110 ZrO_2 (m)	20.35	20.33
011 ZrO_2 (m)	20.70	20.66
−111 ZrO_2 (m)	23.83	23.80
101 ZrO_2 (t)	25.56	25.17
111 ZrO_2 (c)		25.43
111 ZrO_2 (m)	26.54	26.56
100 Zr (hcp)	26.96	26.97
200 ZrO_2 (m)	28.74	28.81
020 ZrO_2 (m)	29.04	29.00
002 ZrO_2 (m)	29.71	29.77
101 Zr (hcp)	30.74	30.78
120 ZrO_2 (m)	32.48	32.47
012 ZrO_2 (m)	33.12	33.19

[22] using Raman spectroscopy have identified the presence of the tetragonal phase in zirconium oxides. Thus, while it is not possible to rule out the presence of cubic zirconia in the oxide scale, the term 'tetragonal' will be used to describe this phase in this paper. Possible reasons for this shift observed between the observed peak and the tetragonal peak in the literature are various, including stress in the oxide and compositional changes from pure ZrO_2.

The monoclinic phase observed in the oxides studied was significantly textured, as observed previously by other researchers [41–43]. Because the diffraction geometry is oriented 90 degrees from the usual frontal orientation, the relative intensity of the peaks differs from that observed from frontal geometry. In particular for the current orientation, the (1 1 1) monoclinic peak is much stronger than the $(\bar{1}\,1\,1)$ monoclinic peak (the 100% peak from a random powder sample).

The amount of tetragonal phase decreases with distance from the oxide–metal interface. Fig. 7 shows three diffraction pattern images taken at 1.25, 5 and 13 μm from the interface in ZIRLO. The intensity of the diffraction ring associated with the tetragonal phase diffraction line decreases with distance from the oxide–metal interface.

Fig. 8 shows a comparison of three diffraction patterns obtained in three different alloys at a fixed distance from the oxide–metal interface (1 μm). The diffraction patterns shown in Figs. 7 and 8 were integrated according to the procedure described in Section 2 and the results are shown below the diffraction patterns. It is visually apparent that the amount of tetragonal phase (arrowed peak) is higher in ZIRLO and Zircaloy-4 than in Zr–2.5%Nb.

Peak fitting of the diffraction patterns (similar to that shown in Fig. 6) was performed to quantify the amount of monoclinic and tetragonal phase present in the oxide. The fitting was performed manually using the PeakFit 4.0 program [44]. The peak shapes were taken to be Pearson VII type and the background was removed using a simple linear model. The peaks used for the fit were those shown in Table 3, with the exception of an extra peak that was introduced to account for the asymmetry of the $(\bar{1}\,1\,1)$ monoclinic peak, which consistently showed a broader tail in the high two-theta side. The peak locations were remarkably consistent throughout the fitting process and the R^2 values (calculated index to measure the quality of the fit) were consistently above 99.99%. One example of such a fit is shown in Fig. 9. The points are the data, the line the fit, the various solid lines underneath are the fitted peaks and the bolded curve at the bottom shows the residuals, which are very small.

This fitting process provided the integrated areas and the full width at half maximum (FWHM) for the peaks considered. Fig. 10 shows the peak intensities for the (1 0 1) tetragonal oxide peak and the (0 2 0) monoclinic peak for the ZIRLO oxide sample, as a function of distance from the oxide–metal interface, after 784 days in 360 °C water. It is clear that there is a periodic pattern for both peaks and that the number of periods corresponds with the observed number of fringes seen in optical microscopy, Fig. 4(d). It is also clear that the peaks are out of phase (when (0 2 0) m is high, the (1 0 1) t is low and vice-versa). This out of phase variation indicates that the periodicity is not caused by cracking or by some geometrical variation that would

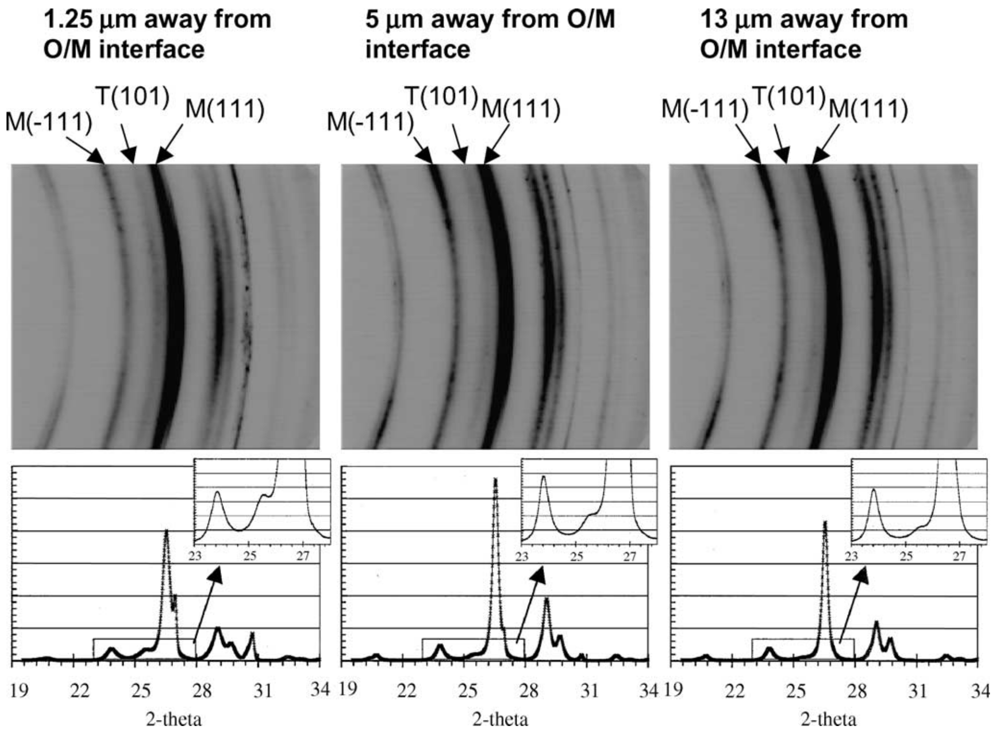

Fig. 7. Diffraction patterns obtained with synchrotron radiation at three different oxide locations from ZIRLO sample exposed to 360 °C water for 784 days (oxide measures 18.1 μm): (a) 1.25 μm (near oxide–metal interface–high tetragonal peak), (b) 5 μm (mid oxide) and (c) 13 μm (outer oxide-low tetragonal peak).

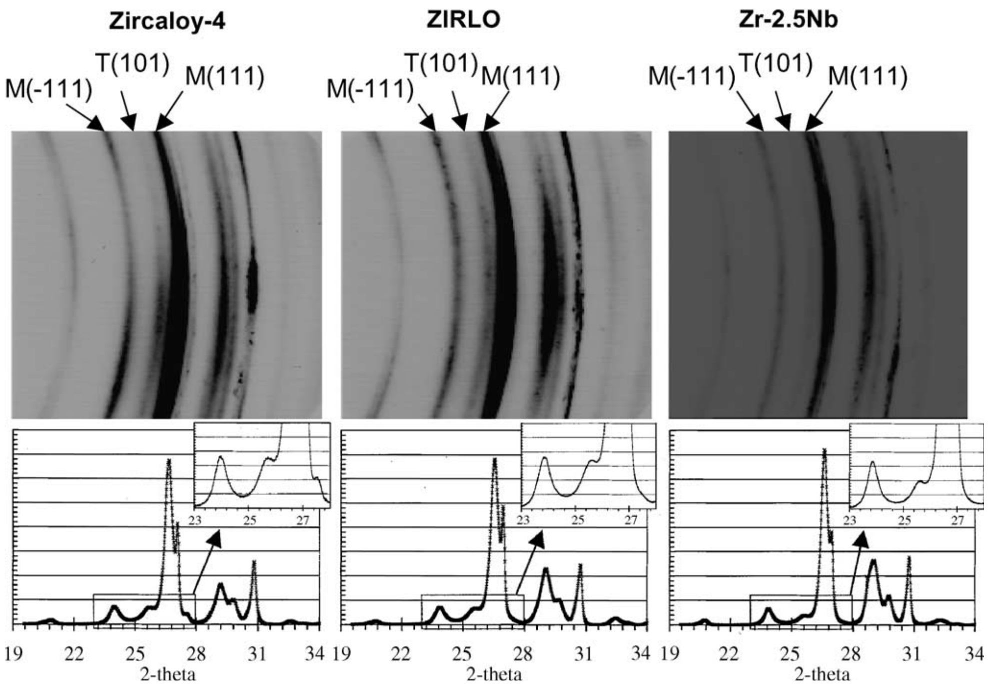

Fig. 8. Diffraction patterns obtained with synchrotron radiation at 1.0 μm from the oxide–metal interface from three alloys exposed to 360 °C water for 784 days (a) Zircaloy-4, (b) ZIRLO, (c) Zr–2.5%Nb.

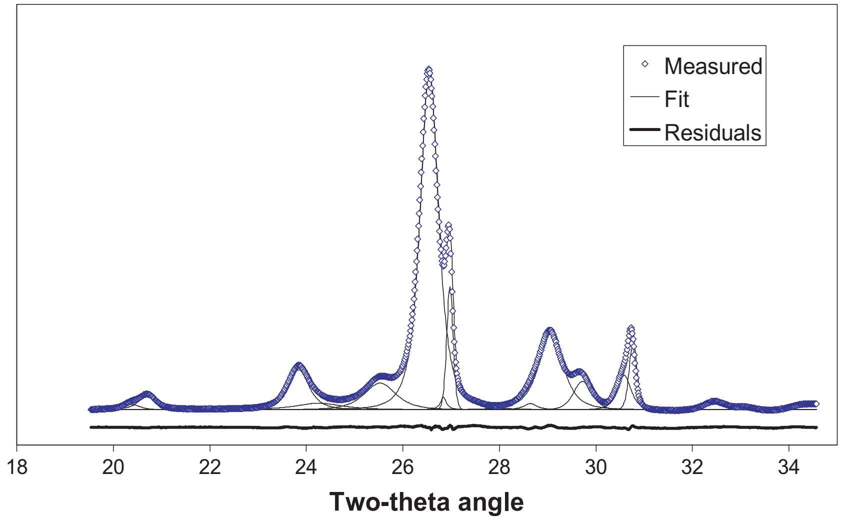

Fig. 9. Peak fit of diffraction pattern taken from oxide at about 1.25 μm from the oxide–metal interface of a ZIRLO sample exposed to 360 °C water for 784 days.

periodically reduce the overall diffracted intensity, but by a real microstructural feature.

To quantify these observations, the tetragonal fraction was calculated using the Garvie–Nicholson formula [45]:

$$f_{\mathrm{T}} = \frac{I^{\mathrm{T}}_{101}}{I^{\mathrm{M}}_{111} + I^{\mathrm{T}}_{101} + I^{\mathrm{M}}_{\bar{1}11}}, \tag{2}$$

where the I^{T}_{101} is the integrated intensity under the (1 0 1) tetragonal peak and the I^{M}_{111} and are $I^{\mathrm{M}}_{\bar{1}11}$ the

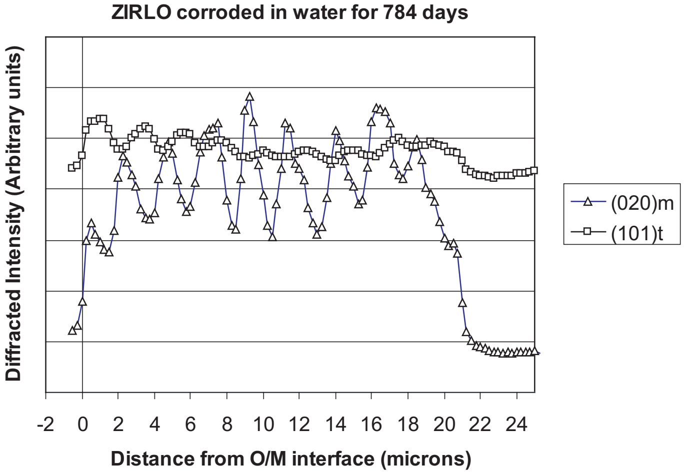

Fig. 10. The peak intensities for the (1 0 1) tetragonal oxide peak and the (0 2 0) monoclinic oxide peak for the ZIRLO sample exposed to 360 °C water for 784 days, as a function of distance from the oxide–metal interface.

corresponding integrated intensities for the (1 1 1) and ($\bar{1}$ 1 1) peaks of the monoclinic phase.

The $f_{\rm T}$ for the various oxides listed in Table 2, were calculated as a function of distance from the oxide–metal interface. Fig. 11 shows the values of $f_{\rm T}$, calculated for the four oxides examined in this work and normalized to the highest value obtained in the four oxides. This highest value occurred in the ZIRLO oxide, and was approximately equal to 15.4%. The tetragonal fraction was highest in the 2–3 microns near the oxide–metal interface and decreased towards the oxide–water interface. The reported error bars correspond to the 95% confidence interval as determined by the fitting and they do not include other possible sources of error, such as imperfect alignment of the beam, surface rugosity, etc.

However, the tetragonal fraction as calculated by the Garvie–Nicholson formula is appropriate for a powder sample, with no texture. An approximate texture correction is performed in this work. For the textured oxides present in Zr-based alloys, Bechade and co-workers obtained pole figures, from which they obtained corrections for the various peaks [43] as a function of χ, the angle between the diffraction plane and surface normal. As a first approximation, the oxides in the present study were assumed to have a texture that was similar to that of Bechade and co-workers. We used a combination of texture measurements by Bechade and co-workers and texture measurements performed in this work in the range of $\chi = 70$–90 degrees. The texture correction was performed by multiplying the measured peak intensity value (which in our geometry is taken at $\chi = 90°$) by the ratio $\gamma^{\alpha}_{\rm hkl}$ defined for phase α and for peak hkl as:

$$\gamma^{\alpha}_{\rm hkl}(\chi) = \frac{\bar{I}^{\alpha}_{\rm hkl}}{I^{\alpha}_{\rm hkl}(\chi)}, \tag{3}$$

where

$$\bar{I}^{\alpha}_{\rm hkl} = \frac{\int_0^{2\pi}\int_0^{\pi/2} I^{\alpha}_{\rm hkl}(\chi,\varphi)\sin\chi\,{\rm d}\chi\,{\rm d}\varphi}{\int_0^{2\pi}\int_0^{\pi/2}\sin\chi\,{\rm d}\chi\,{\rm d}\varphi},$$

where φ is the azimuthal angle and $I^{\alpha}_{\rm hkl}(\chi)$ is the intensity measured in our geometry ($\chi = 90°$).

The intensity correction for each peak is then given by:

$$I^{\alpha,{\rm corr}}_{\rm hkl} = \gamma^{\alpha}_{\rm hkl}(\chi) I^{\alpha,{\rm meas}}_{\rm hkl}, \tag{4}$$

so that the corrected formula is

$$\begin{aligned} f_{\rm T} &= \frac{I^{\rm T,corr}_{101}}{I^{\rm M,corr}_{111} + I^{\rm T,corr}_{10,1} + I^{\rm M,corr}_{\bar{1}11}} \\ &= \frac{\gamma^{\rm T}_{101}(90) I^{\rm T,meas}_{101}}{\gamma^{\rm M}_{111}(90) I^{\rm M,meas}_{111} + \gamma^{\rm T}_{101}(90) I^{\rm T,meas}_{101} + \gamma^{\rm M}_{\bar{1}11}(90) I^{\rm T,meas}_{\bar{1}11}}. \end{aligned} \tag{5}$$

The γ correction factors were obtained using the average intensity values calculated from the research of Bechade [43] and Valot [46], for their oxide grown on zirconium alloys. It should be noted that this assumes (i) that there is no texture gradient in the oxides so intensity values averaged over the oxide thickness can be used and (ii) that the texture does not change greatly with oxide thickness and with alloy type. It should further be noted that the work in Refs. [43,46] was performed near $\chi = 0°$ and thus the information obtained at $\chi = 90°$ has greater experimental uncertainty. Because of all these factors, the variation of $f_{\rm T}$ with distance from the oxide–metal interface and the variation of $f_{\rm T}$ between alloys is emphasized in this work, rather than its absolute value.

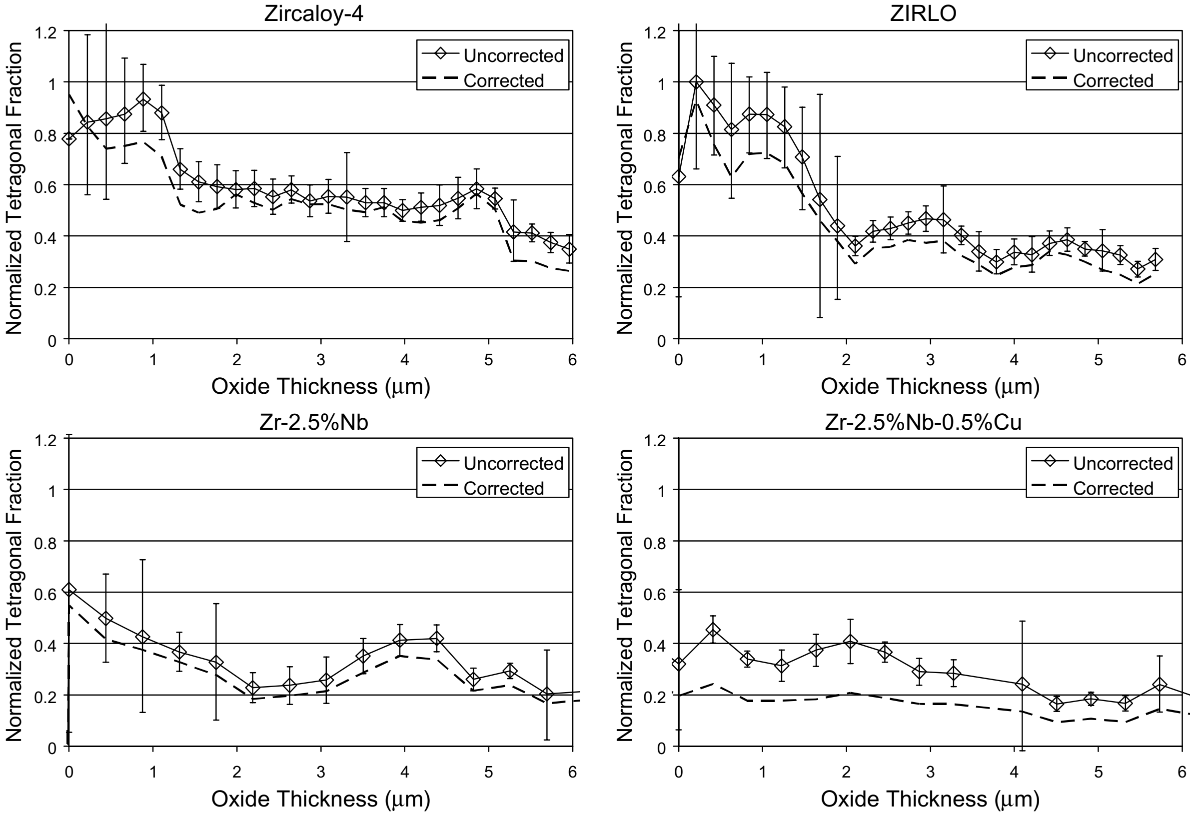

Fig. 11. Tetragonal fraction for the four oxides studied calculated using the uncorrected Garvie–Nicholson formula (solid line) and a modified version (Eq. 5) which corrects for oxide texture, as described in the text (dashed line).

The texture correction factors are then applied to the values of f_T, accordingly. The gamma values utilized for the correction were $\gamma^{M}_{111}(90) = 25$, $\gamma^{T}_{101}(90) = 2.25$ and $\gamma^{M}_{\bar{1}11}(90) = 0.80$. When this correction is applied (dashed lines in Fig. 11), the curves exhibit little change and in shape and in the absolute value of the volume fraction. The highest value decreases to 14.7%, and is now in Zircaloy-4 at the oxide–metal interface.

Among the alloys, higher amounts of tetragonal oxide were found in Zircaloy-4 and ZIRLO than in Zr–2.5%Nb and Zr–2.5%Nb–0.5%Cu. For two of the alloys, the values of f_T appear to be initially low near the oxide–metal interface and increase, reaching a maximum inside the protective layer before decreasing at the end of the layer. However, there is significant uncertainty in the values of f_T for the initial one or two points near the oxide–metal interface, so this trend cannot be confirmed. The higher tetragonal oxide region near the oxide–metal interface has a thickness that roughly corresponds to the thickness of the layers (i.e. 1.8–2.87 μm) observed in the oxide. Further, the calculated values of f_T, periodically increase and decrease with a period similar to the layer thickness, consistent with a repeated process of oxide breakup and rebuilding and suggesting transformation of much of the tetragonal phase in the protective oxide to monoclinic at transition. This is especially evident in the ZIRLO sample.

Other researchers using grazing incidence X-ray diffraction have measured the tetragonal fraction in growing oxides of Zircaloy-4 [41,47] and they generally find values close to 10–15% for Zircaloy-4, near the oxide–metal interface, decreasing to less than 10% in the oxide region located more than 3 μm away from the oxide–metal interface. Bossis and co-workers [40] also see higher tetragonal in Zircaloy-4 than in Zr–1%Nb. Vrtlikova et al. [48] reported a very high percentage of tetragonal zirconia (about 60%) in pre-transition oxides formed in Zr–1%Nb and very little tetragonal phase at similar stages of the oxidation in oxides formed in Zircaloy-4 and in ZIRLO. Béchade and co-workers [49] have measured the tetragonal fraction (averaged over the oxide thickness) in Zircaloy-4 (35%) and Zr1%Nb (15%). This last study also shows that the overall tetragonal fraction is higher in thinner oxides decreasing by a factor of 1.5–2, from an oxide 0.5 μm thick to an oxide 2 μm thick. Thus, the higher percentage of

Table 4
Grain size (nm) in unstressed region of oxide (>3 μm away from oxide–metal interface)

Oxide peak	Zircaloy-4	ZIRLO	Zr–2.5%Nb	Zr–2.5%Nb–0.5%Cu
111m	40	40–45	55–60	55–60
−111m	40	40	45	45
101t	15–20	15	10–15	20

tetragonal oxide seen near the oxide–metal interface is also seen by others and there is a pre-ponderance of observations showing higher tetragonal in Zircaloy-4 than in binary Zr–Nb alloys. The reported observations of the absolute value of the tetragonal fraction varies more widely among researchers and may also be a function of overall oxide thickness in addition to distance from the oxide–metal interface.

Peak broadening was determined from the full-width half maximum (FWHM) obtained from the peak fitting process. Two sources of line broadening need to be considered: strain broadening and small grain size. It is clear that the broadening is significantly higher in the region near the oxide–metal interface. This is logical, since large stresses have been hypothesized in that region. No attempt was made to separate the two contributions to broadening. For regions far from the interface, the particle size is bigger and the stresses should be relaxed (thicknesses > 3 μm). In that region, the contribution of strain broadening should be smaller and thus, the Scherrer formula can be used for calculating grain size. The particle size d is given by the Scherrer equation [38]:

$$d = \frac{0.9\lambda}{B_\theta \cos\theta}, \tag{6}$$

where $B_\theta = (B^2 - B_i^2)^{1/2}$ is the particle size broadening for peak θ, B is the measured peak broadening (FWHM), B_i is the instrumental broadening measured using a standard, θ is the diffraction angle and λ is the wavelength of the synchrotron radiation. Using a pattern measured from a LaB_6 standard obtained from NIST (Standard Reference Material 660a Lanthanum Hexaboride Powder) the instrumental broadening was 0.051 degrees in two-theta. This technique for measuring particle size is useful in the range 0–100 nm, which coincidentally, is the range of interest for the present experiments. It must be noted that the grain size as determined with the methodology described above is best suited to samples having random orientation and nearly equiaxed grain size. Neither of these conditions are satisfied for the oxide sample. However, the grains in oxide films are mostly columnar with the axis normal to the oxide–metal interface [8,10,23–26,33,36]. Therefore, with the geometry of the X-ray beam, sample surface and detector utilized, Fig. 1, the diffracted beams were primarily from poles that were perpendicular to the long axis of the columnar grains. Thus, the grain sizes, at least for the monoclinic phase, were representative of the columnar diameter, or spacing, than of a true equiaxed grain size. However, for simplicity, the term 'grain size' will be used throughout the text to describe the results of the line broadening evaluation.

Table 4 shows the grain sizes in the region far from the oxide–metal interface (>3 μm) for the tetragonal and monoclinic phases in the oxides for the four alloys studied. As can be seen in Table 4, the grain size for the tetragonal phase was typically within the range of 10–20 nm, while the monoclinic grains were in the 40–60 nm range. It is interesting to note that the two alloys that exhibited better autoclave corrosion behavior (Zr–2.5%Nb and Zr–2.5%Nb–0.5%Cu) showed larger monoclinic grain sizes than Zircaloy-4 and ZIRLO. Preliminary TEM observations are in accord with the above results, at least for the comparison between Zr–2.5%Nb and ZIRLO, where the size of the monoclinic grains is larger in the former than in the latter.

4. Discussion

In this work, the first spatially resolved observations of the crystal structure of oxides formed on Zr alloys, performed non-destructively, i.e. in oxides still attached to the base metal, are reported. In contrast, TEM studies, although extremely useful for studying oxide morphology, structure and the phases present (in a qualitative manner), cannot give a quantitative measure of the tetragonal fraction because the thinning process required to make a TEM foil relieves some of the stresses that help stabilize the oxide [22]. Other techniques, such as bulk X-ray diffraction and Raman spectroscopy, examine the oxide as a whole, although some depth resolution can be achieved with glancing angle X-ray diffraction [41,47].

The detailed results, combined with the results of the transmitted light optical microscopy, provide significant evidence for a layered structure in the oxides formed in pure water in the four alloys studied. It is significant that the periods observed in optical microscopy correspond well with the periods observed in the variation of tetragonal phase in the oxide. Additional supporting evidence for a layered structure was observed in the micro X-ray fluorescence results and in cross sectional TEM examinations, which will be published separately.

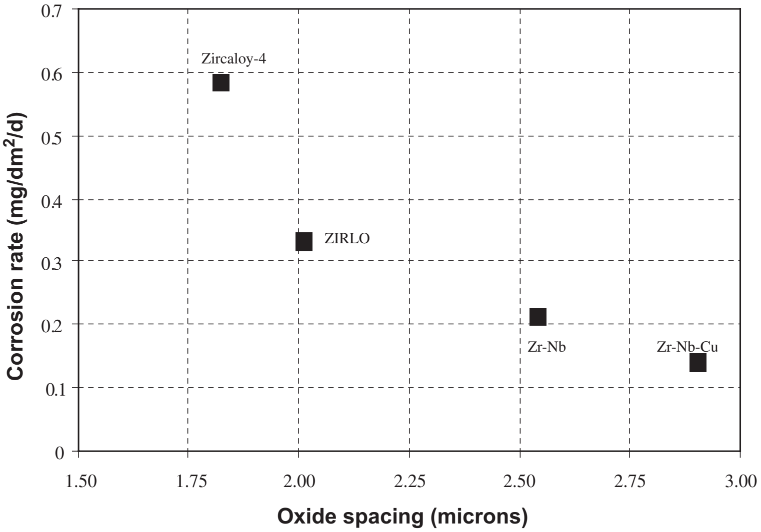

Fig. 12. Post-transition corrosion rate in 360 °C water versus average thickness of oxide layers.

The fact that the layered structure exists in all of the alloys is an indication of a common mechanism of oxide formation and growth in the alloys. Because all of the alloys were exposed together in the same autoclaves and the periods are different for the different oxides, the layers are not related to autoclave shutdowns. The fact that the layers are seen much more clearly and in a wider band in transmitted light than in bright-field illumination indicates that they are not simply a layer of cracks, although the cracking may contribute to their existence and optical contrast. The existence of layers in the oxides formed in Zr-based alloys is consistent with other observations [8,19,22,50,51]. There are many explanations for this optical contrast variation, all associated with periodic variations of the structure of the oxide. Periodic variations in the tetragonal fraction and either the different refractive indexes of the monoclinic and tetragonal oxides or their different defect stoichiometry are possible reasons for the contrast, although the difference in refractive indexes between tetragonal and monoclinic is not very large. The variation in texture associated with the re-formation of a protective layer upon the periodic transitions suffers from the same problem (i.e. the anisotropy in refractive index is not that large). Another possibility is the occurrence of periodic variations in grain size such that the smaller grains absorb more light than the larger grains. Finally, they could be caused by periodic variations in oxide porosity, or cracking. A combination of these two last possibilities (small grain size and more cracking associated with integranular cracking along these small grains) could provide enough scattered intensity that these would appear as darker bands.

Furthermore, it is interesting that this layered structure exhibited a periodicity that varied from alloy to alloy and which correlated to the post-transition corrosion rate. The relationship is shown in Fig. 12, where the post-transition corrosion rate is plotted versus the average layer thickness. The post-transition corrosion rate decreases with increasing oxide layer thickness. This suggests that one of the possible reasons for the differentiated behavior between alloys is that the alloying elements and the alloy microstructure influence the stability of this layer against the processes that cause oxide breakup. The layered structure is consistent with a kinetic corrosion model based on periodic formation and breakdown of a protective oxide film. In that picture the observed layer thickness would correspond to the uncracked, less porous or protective oxide and this layer forms, grows and breaks down cyclically as corrosion proceeds.

It should be noted that any given oxide examined represents a ‘snapshot’ of the corrosion process. To follow the oxidation kinetics it is necessary to examine several snapshots of the same oxide, which is to be done in a later study. In particular, if the oxide transition is related to the transformation of tetragonal oxide to monoclinic oxide [22], then the amount of tetragonal phase in the oxide will vary depending on whether the oxide is examined just before or just after the transition. This uncertainty leads to some variability in the data and comparison between the alloys. Notwithstanding these uncertainties, as the amount of tetragonal phase in the region next to the oxide–metal interface increases, the corrosion rate increases. That is, there is a qualitative correlation in that both the tetragonal fraction and the corrosion rate follow the order:

$$\text{Zircaloy-4} > \text{ZIRLO} > \text{Zr–2.5\%Nb} > \text{Zr–2.5\%Nb–0.5\%Cu}$$

As mentioned above, the above observations are in agreement with those of Bossis et al. [51], Béchade et al. [49] and Petigny et al. [41] who saw higher percentages of tetragonal oxide in Zircaloy-4 than in Zr–1%Nb, but in disagreement with those of Vrtilkova et al. [48] who reported high values of tetragonal fraction (~60%) in Zr–1%Nb but very little in Zircaloy-4 and ZIRLO.

Clearly, the apparent correlation does not indicate whether the higher tetragonal fraction causes the accelerated corrosion rate, whether it results from it, or whether it is a coincidence. The transformation of tetragonal zirconia to monoclinic zirconia is accompanied by a volume increase. When this transformation occurs within the oxide, cracking and micropore formation may result as a result of the local accommodation of the volumetric increase and straining of the surrounding matrix. Assuming that such increased porosity and cracking leads to the oxide transition, the driving force for the transition would be proportional to the amount of tetragonal phase in the pre-transition oxide. In that scenario, those oxides high in tetragonal phase would transform at lower thickness of the protective barrier layer than oxides low in tetragonal phase. Such a mechanism would be consistent with higher corrosion rates in the alloys with high tetragonal phase content in the oxide.

As for the reasons for the different amounts of tetragonal oxide formed in the four alloys, it is noteworthy that the higher Fe alloys had the greatest amount of tetragonal phase and Fe and other transition metals stabilizes the tetragonal phase [31]. However, most of the Fe is tied up in precipitates that are known to be incorporated in metallic form into the oxide [30,31]. The transition metal content of the matrix of these alloys is similar, so it is not clear how these elements could be directly involved in the formation of tetragonal phase.

Because the tetragonal phase content of the oxide was qualitatively proportional to the tin content of the alloys, tin may also play a role in stabilization of the tetragonal phase and there is supporting evidence for this hypothesis. Beie et al. [32] reported about twice the amount of tetragonal phase in the oxide in a Zr–Cr-Fe–Sn alloy containing about 1.2% Sn as in the oxide of a similar alloy containing only 0.5% Sn. These oxides were formed upon exposure to 420 °C steam and had thicknesses of up to 3 μm, thus representing mostly, if not entirely, barrier layer oxide. The higher corrosion rates of the high tin alloy tested by Beie, et al. [32] and the correlation with higher tetragonal fraction in the protective oxide are in agreement with the current results.

The present results indicate that there is a clear benefit to delaying the oxide transition, as this results in lower post-transition corrosion rates. Also observed in all of the alloys, but particularly in the alloys with superior corrosion resistance, was an increase in the size of the monoclinic grains relative to those alloys with lower corrosion resistance.

5. Conclusions

Detailed examinations have been performed of the oxides formed on four different alloys that exhibited a wide range of corrosion behavior in pure water. The objective of the study was to discern structural differences in the oxide that correlate with the post-transition corrosion rates. The structural examinations were performed by use of a combination of microbeam synchrotron radiation and transmitted light optical microscopy. The principal results are as follows:

1. A layered oxide structure was evident in transmitted light optical microscopy in all of the alloys studied. The layers were extremely regular (constant period) and extended over the whole oxide thickness. The regularity of the layered structures indicates that corrosion process is the same from the beginning to the end of the corrosion test.
2. Comparing the layer periodicity from alloy to alloy, the average spacing between layers was inversely proportional to the post-transition corrosion rate, indicating a clear benefit to delaying the oxide transition.
3. Detailed diffraction experiments showed the presence of both monoclinic and tetragonal oxide. The percentage of tetragonal oxide was highest in the first couple of microns near the interface and was higher in Zircaloy-4 than in ZIRLO. The tetragonal fraction in both of these alloys was higher than in the Zr–Nb–Cu alloys.
4. The samples with higher tetragonal oxide fraction in the first few of microns near the oxide–metal interface exhibited the higher corrosion rate. The tetragonal and monoclinic oxide peak intensities showed alternate periodic variations in the oxide layer, in agreement with the layered structure seen in optical microscopy.
5. These new observations, coupled with published information, suggest that the formation of the tetragonal phase and its decomposition to the monoclinic structure, play a significant role in the corrosion kinetics of Zr-based alloys.
6. The final oxide grain size was in the range 40–60 nm for the monoclinic phase, while the tetragonal oxide grains were about 15–20 nm. The Zr–2.5%Nb and Zr–2.5%Nb–0.5%Cu alloys exhibited larger monoclinic grain sizes than the Zircaloy-4 and ZIRLO samples.

Acknowledgements

The authors would like to thank Sarah Jurgensmeier (Penn State) and Jonna Partezana (Westinghouse) for assistance with the experiments and Marcelo Silva (Penn State) for assistance with the peak fitting effort. We also thank Randy Lott of Westinghouse and Jean-Luc Béchade of CEA-Saclay for many helpful discussions. Use of the Advanced Photon Source was supported by the US Department of Energy, Basic Energy Sciences, Office of Science, under Contract No. W-31-109-Eng-38. This research was sponsored by the Department of Energy, Nuclear Engineering Research Initiative (DOE-NERI) program, under grant number DE-FC03-99SF21918.

References

[1] G.P. Sabol, G.R. Kilp, M.G. Balfour, E. Roberts, Eighth International Symposium on Zirconium in the Nuclear Industry, ASTM STP 1023, San Diego, 1989, p. 227.
[2] A.V. Nikulina, V.A. Markelov, M.M. Peregud, Y.K. Bibilashvili, V.A. Kotrekhov, A.F. Lositsky, N.V. Kuzmenko, Y.P. Shevnin, V.K. Shamardin, G.P. Kobylyansky, A.E. Novoselov, Zirconium in the Nuclear Industry: Eleventh International Symposium, ASTM STP 1295, Garmisch-Partenkirchen, Germany, 1996, p. 785.
[3] F. Garzarolli, E. Steinberg, H.G. Weidinger, Zirconium in the Nuclear Industry: Eighth International Symposium, ASTM STP 1023, San Diego, CA, USA, 1989, p. 202.
[4] G.R. Kilp, D.R. Thornburg, R.J. Comstock, IAEA Technical Committee Meeting on Fundamental Aspects of Corrosion on Zirconium Base Alloys in Water Reactor Environments, IAEA IWGFPT/34, Portland, OR, USA, 1990, p. 145.
[5] A. Garde, S.R. Pati, M.A. Krammen, G.P. Smith, R.K. Endter, Zirconium in the Nuclear Industry: Tenth International Symposium, ASTM STP 1245, Baltimore, MD, USA, 1994, p. 760.
[6] J.P. Mardon, D. Charquet, J. Senevat, 12th International Symposium on Zr in the Nuclear industry, ASTM STP 1354, Toronto, 2000, p. 505.
[7] J.E. LeSurf, Application Phenomena for Zirconium and its Alloys, ASTM STP 458, 1969, p. 286.
[8] G.P. Sabol, S.G. McDonald, Stress Effects and the Oxidation of Metals, American Institute of Mining, Metallurgical and Petroleum Engineers, New York, NY, 1975, p. 353.
[9] B. Cox, J. Nucl. Mater. 29 (1969) 50.
[10] B. Cox, A. Donner, J. Nucl. Mater. 47 (1973) 72.
[11] D.E. Thomas, in: B. Lustman, F. Kerze Jr. (Eds.), Metallurgy of Zirconium, McGraw-Hill, New York, 1955, p. 608.
[12] S. Kass, Symposium on Corrosion of Zirconium Alloys, ANS Winter meeting, ASTM STP 368, New York, 1963, 1964, p. 3.
[13] K. Hauffe, Oxidation of Metals, Plenum, New York, 1965.
[14] S. Kass, J. Nucl. Mater. 29 (1969) 315.
[15] G.P. Sabol, S.B. Dalgaard, J. Electrochem. Soc. 122 (1975) 316.
[16] B. Griggs, H.P. Maffei, D.W. Shannon, J. Electrochem. Soc. 109 (1962) 665.
[17] A.A. Kiselev, V.A. Myshkin, A.V. Kozhevnikov, S.L. Korolev, E.G. Shorina, in: Corrosion of Reactor Materials, vol. 2, IAEA, Vienna, 1962, p. 67.
[18] D.H. Bradhurst, P.M. Heuer, J. Nucl. Mater. 37 (1970) 35.
[19] G.P. Sabol, S.G. McDonald, G.P. Airey, Zirconium in Nuclear Applications, ASTM STP 551, 1974, p. 435.
[20] B. Cox, Rate Controlling Process During the Oxidation of Zirconium Alloys, Atomic Energy of Canada, 1967, AECL-2777.
[21] B. Cox, J. Nucl. Mater. 28 (1968) 1.
[22] J. Godlewski, J.P. Gros, M. Lambertin, J.F. Wadier, H. Weidinger, Ninth International Symposium on Zr in the Nuclear Industry, ASTM STP 1132, Kobe, Japan, 1991, p. 416.
[23] K. Takeda, H. Anada, Twelfth International Symposium on Zr in the Nuclear Industry, ASTM STP 1354, Toronto, Canada, 2000, p. 592.
[24] B. Wadman, H.-O. Andren, Zirconium in the Nuclear Industry: Ninth International Symposium, ASTM STP 1132, Kobe, Japan, 1991, p. 461.
[25] B. Wadman, Z. Lai, H.O. Andren, N. A-E., P. Rudling, Pettersson, Tenth International Symposium on Zr in the Nuclear Industry, ASTM STP 1245, Baltimore, 1994, p. 579.
[26] H. Anada, B.J. Herb, K. Nomoto, S. Hagi, R.A. Graham, T. Kuroda, Eleventh ASTM Symposium on Zr in the Nuclear Industry, ASTM STP 1295, 1996, p. 74.
[27] D. Pecheur, J. Godlewski, P. Billot, J. Thomazet, Eleventh International Symposium on Zr in the Nuclear Industry, ASTM STP 1295, Garmisch-Partenkirchen, 1995, p. 94.
[28] F. Garzarolli, H. seidel, R. Tricot, J.P. Gros, Zirconium in the Nuclear Industry: Ninth International Symposium, ASTM STP 1132, Kobe Japan, 1991, p. 395.
[29] B. Cox, J. Nucl. Mater. 41 (1971) 96.
[30] D. Pecheur, F. Lefebvre, A.T. Motta, C. Lemaignan, D. Charquet, Tenth International Symposium on Zirconium in the Nuclear Industry, ASTM STP 1245, Baltimore, MD, 1994, p. 687.
[31] D. Pecheur, F. Lefebvre, A.T. Motta, C. Lemaignan, J.-F. Wadier, J. Nucl. Mater. 189 (1992) 2318.
[32] H.-J. Beie, A. Mitwalsky, F. Garzarolli, H. Ruhmann, H.-J. Sell, Tenth International Symposium on Zr in the Nuclear Industry, ASTM STP 1245, Baltimore, 1993, p. 615.
[33] IAEA, Corrosion of Zirconium Alloys in Nuclear Power Plants, IAEA, Vienna IAEA-TECDOC-684, 1993.
[34] J.H. Baek, Y.H. Jeong, I.S. Kim, J. Nucl. Mater. 280 (2000) 235.
[35] C. Lemaignan, A.T. Motta, in: B.R.T. Frost (Ed.), Zirconium in Nuclear Applications, Nucl. Mater., vol. 10B, VCH, New York, 1994, p. 1.
[36] IAEA, Waterside Corrosion of Zirconium Alloys in Nuclear Power Plants, International Atomic Energy Agency, Vienna TECDOC996, 1998.
[37] Z. Cai, B. Lai, W. Yun, P. Ilinski, D. Legnini, J. Maser, W. Rodrigues, The Sixth International Conference for X-Ray Microscopy, AIP Proceedings 507, 2000, p. 472.

[38] B.D. Cullity, Elements of X-ray Diffraction, Addison-Wesley, Reading, MA, 1978.

[39] H.G. Weidinger, H. Ruhmann, G. Cheliotis, M. Maguire, T.-L. Yau, Ninth International Symposium on Zr in the Nuclear Industry, ASTM STP 1132, 1991, p. 499.

[40] P. Bossis, G. Lelievre, P. Barberis, X. Iltis, F. Lefebvre, Twelfth International Symposium on Zirconium in the Nuclear Industry, ASTM STP 1354, Toronto, 2000, p. 918.

[41] N. Petigny, P. Barberis, C. Lemaignan, C. Valot, M. Lallemant, J. Nucl. Mater. 280 (2000) 318.

[42] C. Valot, D. Ciosmak, M.T. Mesner, M. Lallemant, Oxidation of Metals 48 (1997) 329.

[43] J.L. Bechade, R. Dralet, P. Goudeau, P. Yvon, Materials Science Forum 347–349 (2000) 471;
J.L. Bechade, personal communication, 2003.

[44] PeakFit, 4.0 for Windows ed: SPSS Chicago, IL, USA, 1997.

[45] R.C. Garvie, P.S. Nicholson, J. Am. Ceram. Soc. 55 (1972) 303.

[46] R. Valot, PhD thesis; University of Burgundy, France, 1995.

[47] H.G. Kim, T.H. Kim, Y.H. Jeong, J. Nucl. Mater. 306 (2002) 44.

[48] V. Vrtlikova, J. Jaros, J. Cmakal, L. Belovsky, International Topical Meeting on LWR Fuel Performance, ANS, Park City, UT, 2000, p. 401.

[49] J.L. Bechade, R. Dralet, P. Goudeau, P. Yvon, Materials Science Forum 347–349 (2000) 471.

[50] H. Anada, K. Takeda, Zirconium in the Nuclear Industry, Eleventh International Symposium, ASTM STP 1295, 1996, p. 35.

[51] P. Bossis, J. Thomazet and F. Lefebvre, Zirconium in the Nuclear Industry: Thirteenth International Symposium, 2001; ASTM STP 1423, Annecy, France, 190-221.